Agricultural and Forest Meteorology xxx (xxxx) xxx–xxx

Contents lists available at ScienceDirect

Agricultural and Forest Meteorology

journal homepage: www.elsevier.com/locate/agrformet

Dependence of thermal roughness length on friction velocity across land cover types: A synthesis analysis using AmeriFlux data

Angela Rigden*, Dan Li, Guido Salvucci

Department of Earth and Environment, Boston University, 675 Commonwealth Ave., Boston, MA 02215, USA

ARTICLE INFO

Keywords:
Thermal roughness length
Excess resistance
kB^{-1}
Sensible heat flux

ABSTRACT

Using AmeriFlux data from 74 eddy covariance sites, we present a synthesis of the dependence of thermal roughness length on friction velocity across five land covers types, including deciduous broadleaf forests, evergreen needleleaf forests, croplands, grasslands, and shrublands. To analyze patterns in thermal roughness length, we estimate the ratio of momentum to thermal roughness lengths (kB^{-1}) at half hourly scales. Because kB^{-1} cannot be directly measured, we infer kB^{-1} from surface flux and meteorological measurements using Monin-Obukhov similarity theory. The inferred kB^{-1} is moderately correlated with the measured friction velocity over two of the land cover types—grasslands and shrublands—but weakly correlated at croplands and forests, suggesting that kB^{-1} varies with friction velocity over bluff body surfaces, but not over tightly packed, permeable canopies, such as forests and croplands. This is consistent with previous work showing contrasting turbulent structures over sparse and dense vegetation canopies. To determine how this degree of correlation affects the modeling of kB^{-1}, we estimate kB^{-1} using four common models, specifically those with friction velocity dependencies, and find that no single model works the best across land covers.

1. Introduction

Accurate estimates of turbulent fluxes of momentum, heat, and water vapor from the surface are critical for simulating atmospheric dynamics. Turbulent transport near the surface is often represented using an analogue to the transfer of electrical charge as described by Ohm's law, such that the turbulent flux and driving gradient are analogous to the electrical current and potential, respectively (Monteith and Unsworth, 2013). This resistance analogue is useful when describing turbulent fluxes as electrical current theory is well established, and facilitates the modeling of complex networks, i.e. resistance in series and/or in parallel. Using a resistance analogue, sensible heat flux (H) is described as:

$$H = \frac{-\rho c_p \cdot (T_a - T_s)}{r_{aH}} \quad (1)$$

In Eq. (1), ρ is the air density, c_p is the specific heat of air at constant pressure, T_a is the air temperature measured at height z, T_s is the temperature at the apparent source/sink height, and r_{aH} is the aerodynamic resistance to sensible heat transfer between the apparent height of the source/sink and height z.

Often, the source/sink height of heat is parameterized as a function of the sink height of momentum. For aerodynamically smooth surfaces, the transfer of momentum and heat are both controlled by diffusive forces (i.e. viscosity). Under such conditions, the apparent source/sink heights for heat and momentum are similar. Over rough surfaces, the sink of momentum is assumed to be the height at which the extrapolated wind speed from the logarithmic profile goes to zero, or at $z_o + d$, where z_o is the momentum roughness height and d is the zero-plane displacement height. The source/sink height of heat is assumed to be the height at which the extrapolated temperature equals the surface radiometric temperature, or at $z_{oh} + d$, where z_{oh} is the thermal roughness height. Since pressure forces dominate the transfer of momentum while the transfer of heat remains controlled by viscous forces over rough surfaces (Thom, 1972), the sink height for momentum is typically higher than the source/sink height of heat, i.e. $z_o > z_{oh}$, reflecting more efficient momentum transfer by pressure forces. Over vegetated or partially vegetated surfaces, the distribution of sources/sinks of momentum and heat are also spatially variable, leading to further divergence of heat and momentum roughness lengths. In addition to structural characteristics of the vegetation (LAI, vegetation flexibility, canopy height, fraction of soil cover) modifying the distribution of sources/sinks, roughness lengths have also been found to vary with the degree of water stress and climate conditions, specifically over sparse canopies (Lhomme et al., 1997).

To account for these differences between heat and momentum

* Corresponding author.
E-mail address: ajrigden@bu.edu (A. Rigden).

http://dx.doi.org/10.1016/j.agrformet.2017.06.003
Received 1 February 2017; Received in revised form 19 May 2017; Accepted 5 June 2017
0168-1923/ © 2017 Elsevier B.V. All rights reserved.

transfer, heat transfer is often modeled using an excess resistance (r_b), such that $r_{aH}(z_{oh} \rightarrow z) = r_{aH}(z_o \rightarrow z) + r_b$, where $r_a(z_o \rightarrow z)$ represents the turbulent aerodynamic resistance for heat integrated to z_o and,

$$r_b = \frac{\left[\ln\left(\frac{z_o}{z_{oh}}\right)\right]}{ku_*} \tag{2}$$

In Eq. (2), k is the von Karman constant and u_* is the friction velocity. This common representation (Eq. (2)) ignores any influence of stability corrections over the small region $z_o \rightarrow z_{oh}$. Eq. (2) is often rearranged in terms of the inverse Stanton number (B^{-1}) and the parameter kB^{-1} is defined as (Chamberlain, 1966; Owen and Thomson, 1963),

$$kB^{-1} = kr_b u_* = \ln\left(\frac{z_o}{z_{oh}}\right) \tag{3}$$

From Eq. (3), z_{oh} can be parameterized as a function of kB^{-1}, such that,

$$z_{oh} = \frac{z_o}{\exp(kB^{-1})} \tag{4}$$

As seen in Eq. (4), kB^{-1} is a parameter that acts to reduce z_o exponentially to estimate z_{oh}. The parameter z_{oh} is a critical input to land surface models, and is especially important when estimating processes at the land surface that depend on surface temperature, such as stomatal conductance. Thus, tremendous effort has been made to parameterize this proportionality constant, kB^{-1} (see reviews by Massman, 1999; Verhoef et al., 1997); however, no universal scaling and parameterization have been agreed upon. Models of kB^{-1} vary in complexity, including simplified parameterizations treating kB^{-1} as a constant, perhaps dependent on land cover, more complex parameterizations that depend on u_* and/or z_o (e.g. Brutsaert, 1982; Kanda et al., 2007; Yang et al., 2008; Zilitinkevich, 1995), models that incorporate vegetation fraction, canopy structure, and/or canopy density (e.g. Blumel, 1999; Massman, 1999; Yang and Friedl, 2003), and machine learning algorithms trained on eddy covariance data (Chaney et al., 2016).

In this study, we focus on characterizing the dependence of kB^{-1} on u_* across land cover types. Our aim is not to develop a new parameterization, but to reexamine the dependence of thermal roughness length (through kB^{-1}) on friction velocity using an unprecedented amount of data. We utilize the AmeriFlux network of eddy covariance data to synthesize the relationship between kB^{-1} on u_* at evergreen needleleaf forests, broadleaf deciduous forests, croplands, grasslands, and shrublands. Our three main objectives are to (1) estimate half-hourly kB^{-1} from measured sensible heat flux and meteorological variables, (2) determine the correlation between u_* and kB^{-1} by land cover type, and (3) evaluate commonly used models of kB^{-1}. To minimize the effect of vegetation phenology on our results, we focus the analysis during the summertime, which we define as June, July, and August.

2. Materials and methods

2.1. Inferring kB^{-1} from observations

To estimate kB^{-1}, we used summertime data from 74 eddy covariance sites within the AmeriFlux data network (data available at http://www.ameriflux.lbl.gov; additionally, see link for a map of all sites). Table S1 presents the full list of sites used in this study with corresponding latitude, longitude, and land cover classification. To facilitate our analysis, we aggregated the sites by land cover types. In particular, we focused on shrublands (SHR, N (number of sites) = 8), grasslands (GRA, N = 17), croplands (CRO, N = 13), deciduous broadleaf forests (DBF, N = 11), and evergreen needle leaf forests (ENF, N = 25). In the shrubland classification, we included open shrublands, woody savannas, and savannas. Note, the "shrubland" land cover types are defined by the International Geosphere–Biosphere Programme (IGBP) as less densely vegetated than forests, with open shrublands defined as shrub canopy cover between 10% and 60%, woody savannas as forest canopy cover between 30% and 60%, savannas as forest canopy cover between 10% and 30%. All AmeriFlux Level-2 data were processed following Rigden and Salvucci (2015).

To estimate kB^{-1}, we combined Eqs. (1) and (3), and the fact that $r_{aH}(z_{oh} \rightarrow z) = r_{aH}(z_o \rightarrow z) + r_b$, as,

$$kB^{-1} = k\cdot\left(\frac{-\rho c_p(T_a - T_{sr})}{H} - r_{aH}(z_o \rightarrow z)\right)\cdot u_* \tag{5}$$

In Eq. (5), T_{sr} represents the surface radiometric temperature, which was estimated primarily from upwelling longwave radiation (R_{lu}) following the Stephan Boltzmann relation as,

$$T_{sr} = \left(\frac{R_{lu} - (1-\varepsilon)R_{ld}}{\varepsilon\sigma}\right)^{1/4} \tag{6}$$

In Eq. (6), σ is the Stefan-Boltzmann constant, ε is the emissivity, and R_{ld} is the downwelling longwave radiation. To estimate $r_{aH}(z_o \rightarrow z)$, we utilized Monin Obukhov similarity theory (Brutsaert, 2005; Garratt, 1994) neglecting the stability correction from z_{oh} to z_o, as previously mentioned, as,

$$r_{aH}(z_o \rightarrow z_m) = \frac{1}{u_* k}\left[\ln\left(\frac{z_m - d}{z_o}\right) - \Psi_h\left(\frac{z_m - d}{L}\right) + \Psi_h\left(\frac{z_o}{L}\right)\right] \tag{7}$$

In Eq. (7), z_m is the measurement height and L is the Obukhov length, defined as,

$$L = \frac{-u_*^3 \rho T_a\cdot(1 + \eta q_a)\cdot c_p}{kgH} \tag{8}$$

In Eq. (8), η (= 0.61) is the dimensionless ratio of the gas constants for dry air to water vapor and g is the gravitational acceleration. The Businger–Dyer stability function for heat (Ψ_h), which accounts for deviations of the temperature profile due to stabilizing or destabilizing thermal stratification, was calculated from the dimensionless stability parameter $\xi = z_m/L$ following (Brutsaert, 2005; Garratt, 1994),

$$\Psi_h = \begin{cases} 2\ln[(1 + \sqrt{1 - 16\xi})/2] & \xi < 0 \\ -5\xi & 0 \le \xi \le 1 \\ -5 - 5\ln(\xi) & \xi > 1 \end{cases} \tag{9}$$

Note, in Eqs. (5)–(9), all variables are either measured (H, T_a, R_{lu}, ρ, q_a, u_*) or constants (k, g, c_p, η) except z_o, d, and ε. To estimate z_o and d, we assumed z_o to be 10% of the vegetation height (z_{veg}) and d to be 70% of z_{veg}. To more accurately characterize z_{veg}, for each site we determined the climatological monthly z_{veg} (ranging from 0 to z_m) that best predicted the measured wind speed assuming atmospheric neutrality following Pennypacker and Baldocchi (2016). To account for the effect of ε, we performed the analysis over a range of ε values from 0.94 to 0.98.

When analyzing the diurnal cycles of kB^{-1}, we excluded half-hours with counter-gradient heat fluxes, e.g. $H > 0$ when $T_s < T_a$, which sometimes occurred during early morning and afternoon transitional periods. Friction velocities less than 0.01 m/s were also excluded from the analysis. Additionally, to minimize errors associated with small temperature gradients, we excluded half-hours when H was less than 20 Wm^{-2}. The total amount of data used in this analysis is located in Table 1. When determining the relationship between kB^{-1} and u_*, we further subsampled the data to minimize errors associated with small temperature gradients. Specifically, we subsampled the data to include only the 8 half-hours with the largest sensible heat flux for each day. Lastly, as another quantitative tool to assess the strength of the relationship between kB^{-1}, r_b, and u_*, we fit a power model to the subsampled half-hourly data, in the form $r_b = a(u_*^{P1})$ and $kB^{-1} = b(u_*^{P2})$, using a robust linear regression in the logarithmic space.

Table 1
Total number of sites and amount of data for each land cover type ($\varepsilon = 0.98$). The "total amount of data" includes half hours when $H > 20\ Wm^2$, $u_* > 0.01ms^{-1}$, and no counter-gradient heat fluxes. Recall, when determining the relationship between kB^{-1} and u_* (as demonstrated in Fig. 2 and Fig. 3), the data is further subset to include only the 8 half-hour of maximum H during that day. This subsetting routine reduces the total number of observations across all land covers by almost half (from 532,546 to 254,980 half hour observations).

Land Cover Type	Number of Sites (N)	Total amount of data (number of half hours)
Shrubland (SHR)	5	81,985
Grasslands (GRA)	17	140,186
Croplands (CRO)	13	72,106
Deciduous Broadleaf Forest (DBF)	11	62,306
Evergreen Needleleaf Forest (ENF)	25	175,963

2.2. Parameterizations of kB^{-1}

To further explore the relationship between kB^{-1} and u_*, we estimated kB^{-1} using established models. Because we were primarily interested in the dependence of kB^{-1} on u_*, we focused on models with explicit u_* dependence. Frequently, models relate kB^{-1} to u_* through the roughness Reynolds number (Re_*), which is defined as $Re_* = z_o u_*/\nu$, where ν is kinematic viscosity (Brutsaert, 1982; Kanda et al., 2007; Zilitinkevich, 1995). We focused on two functional forms of power functions, as follows:

$$kB^{-1} = C_1 Re_*^{0.25} - 2 \tag{10}$$

$$kB^{-1} = C_2 Re_*^{0.5} \tag{11}$$

Eq. (10) was first proposed by Brutsaert (1982) with $C_1 = 2.46$ and was re-parameterized by Kanda et al. (2007) such that $C_1 = 1.29$. Eq. (11) was proposed by Zilitinkevich (1995) with $C_2 = 0.1$. We also estimated kB^{-1} using the model of Yang et al. (2008), which is based on friction temperature (θ_*) in addition to u_* as,

$$z_{oh} = \frac{70\nu}{u_*} \cdot \exp(-C_3 u_*^{0.5} \theta_*^{0.25}) \tag{12}$$

where θ_* is defined as,

$$\theta_* = \frac{\theta_a u_*^2}{kgL} \tag{13}$$

In Eq. (12), θ_a is the potential temperature of the air. Yang et al. (2008) estimated $C_3 = 7.2$.

Lastly, we applied a leaf boundary layer model (Defraeye et al., 2013; Parlange and Waggoner, 1972; Parlange et al., 1971), which depends on the leaf scale Reynolds number, $Re_{leaf} = u_{leaf} L_w/\nu$ where u_{leaf} is the extrapolated wind speed at the source height and L_w is the characteristic scale of the leaves, which we refer to as the "leaf width". For this model, we assume that the vegetation top, or z_{veg}, is the source height, and define the excess resistance at the leaf (r_{bL}) according to the leaf boundary layer height (Defraeye et al., 2013). For forced-convective laminar and turbulent flow, the models for r_{bL} are, respectively, as follows:

$$r_{bL1} = \frac{L_{w1}}{\alpha \cdot (N_1 Pr^{1/3} Re_{leaf}^{1/2})} \tag{14}$$

$$r_{bL2} = \frac{L_{w2}}{\alpha \cdot (N_2 Pr^{0.43} Re_{leaf}^{0.8})} \tag{15}$$

In Eqs. (14) and (15), α is the thermal diffusivity of air ($= k_v/(\rho c_p)$, where k_v is the thermal conductivity of air), Pr is the Prandtl number ($= \nu/\alpha$), and N_x is a scaling coefficient. We calibrated the scaling coefficients N_1 and N_2 from 0.332 and 0.032 (Defraeye et al., 2013) to 1 and 0.20, respectively, to rescale L_w. Because we set the source height to be the vegetation height, which is above $z_o + d$, we define a new aerodynamic resistance from $z_{veg} - d$ to $z_m - d$ (rather than from $z_o + d$ to $z_m - d$), which we refer to as $r_{aH,z_{veg}\to z_m}$, as,

$$r_{aH,z_{veg}\to z_m} = \frac{1}{u_* k} \ln\left(\frac{z_m - d}{z_{veg} - d}\right) = \frac{1}{u_* k} \ln\left(\frac{z_m - d}{z_o}\right) + \frac{1}{u_* k} \ln\left(\frac{z_o}{z_{veg} - d}\right) \tag{16}$$

To put these resistance in terms of kB^{-1}, we rely on the definition of r_{aH} (neglecting stability correlations), which is,

$$r_{aH} = \frac{1}{u_* k} \ln\left(\frac{z_m - d}{z_{oh}}\right) \tag{17}$$

If we model the total resistance as a series of the "excess" leaf resistance and resistance from $z_m \to z_{veg}$, such that $r_{aH} = r_{bL} + r_{aH,z_{veg}\to z_m}$, kB^{-1} can be estimated by combining Eq. (3) and Eqs. (14)–(17) as,

$$kB^{-1} = u_* k r_{bL} - \ln\left(\frac{z_{veg} - d}{z_o}\right) \tag{18}$$

We refer to this model as the "leaf boundary layer" model. It is similar in form to Eq. (3), but includes the offsetting constant term $\ln\left(\frac{z_{veg} - d}{z_o}\right)$.

2.3. Assessing the performance of kB^{-1} parameterizations

To assess the performance of each kB^{-1} model, we calculated the root mean square error (RMSE) of the predicted surface temperature (by rearranging Eqs. (5)–(19), as shown below) and the inferred T_{sr} (Eq. (6)) during the daytime ($H > 20\ \mathrm{Wm}^{-2}$). Note, when Eq. (5) is rearranged, T_s can be estimated as a function of kB^{-1} as,

$$T_s = \frac{H \cdot \left(r_{aH} + \left(\frac{kB^{-1}}{u_* k}\right)\right)}{\rho c_p} + T_a \tag{19}$$

For each site, we calibrated the coefficients C_1, C_2, C_3, L_{w1} and L_{w2} to minimize the RMSE of predicted versus observed surface temperature. Additionally, for each site we determined a constant kB^{-1} value and a constant z_{oh} value that minimize the RMSE of T_s.

3. Results

In the following, we present results primarily for $\varepsilon = 0.98$; however, the following results are consistent with those using two other emissivity values ($\varepsilon = 0.94$ and $\varepsilon = 0.96$), as demonstrated in Appendix A. All results are aggregated by land cover type.

3.1. Diurnal scale variations

To assess diurnal variations in the thermal roughness length, we analyzed both r_b and kB^{-1}, as variations of z_{oh} from z_o are reflected in both variables (Eq. (3)). Recall $kB^{-1} = kr_b u_*$ (Eq. (3)); thus, it is of interest to look at how both r_b and kB^{-1} vary with u_*. It became immediately apparent that across all vegetation types, the nighttime magnitudes of kB^{-1} and r_b are strongly sensitive to emissivity (Fig. S1–S3); thus, we focused our attention on the daytime dynamics, which are less sensitive to emissivity. The daytime variations of r_b, u_*, and kB^{-1} for each land cover type are shown in Fig. 1 for $\varepsilon = 0.98$. As expected, we see a diurnal pattern during the daytime in u_*, with the largest u_*occurring midday.

In this paper, we are particularly interested in exploring how both r_b and kB^{-1} vary with u_*. During the daytime hours, r_b, kB^{-1}, and u_* tend to vary during the daytime, with the degree of variation dependent on land cover type, as shown in Fig. 1. At shrublands and grasslands, our results show that kB^{-1} has a diurnal cycle, increasing throughout the morning and decreasing in the evening. These daytime dynamics in kB^{-1} over shrublands and grasslands parallel the daytime dynamics of

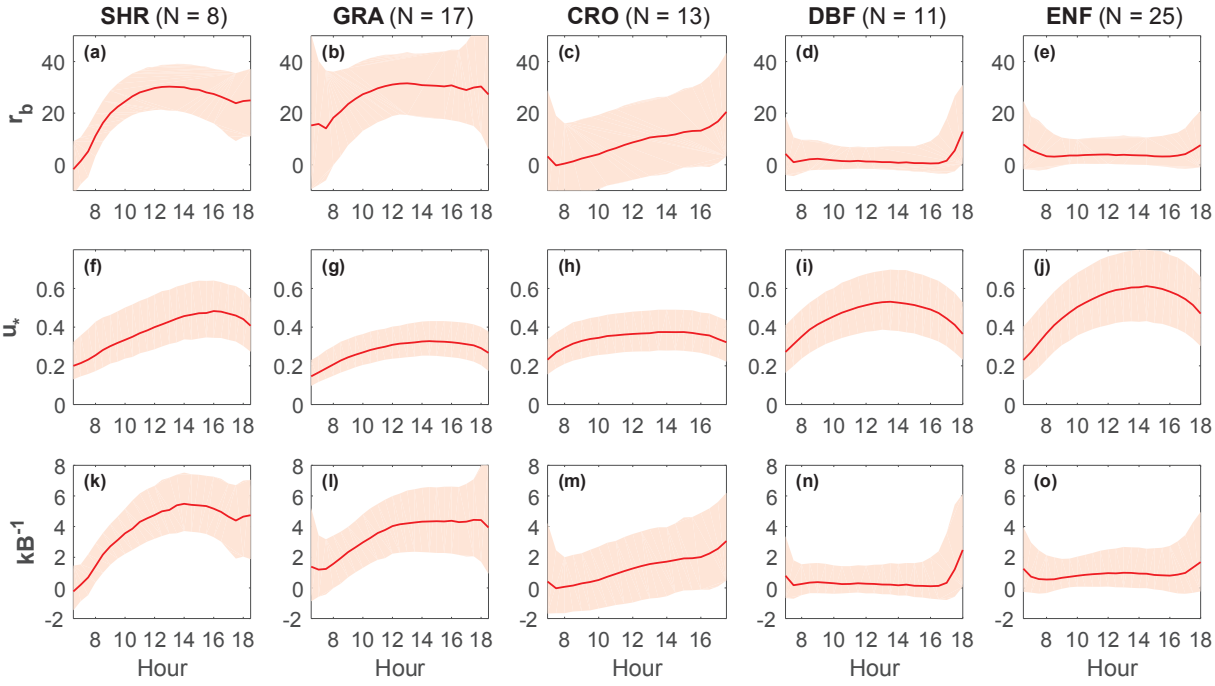

Fig. 1. The daytime diurnal cycle of summertime (a-e) r_b [s/m], (f-j) u_* [m/s], and (k-o) kB^{-1} [unitless] across five land-covers (columns) with $\varepsilon = 0.98$. The red line represents the median diurnal cycle across all sites, with the shaded region indicating the 25th and 75th percentile for each half hour. The number of sites (N) for each land cover type is indicated in the title. In Fig. 1, data is plotted for the hours in which the climatological diurnal cycle of $H > 20 Wm^{-2}$. Similar figures with nighttime included are shown in Appendix A for $\varepsilon = 0.94$, $\varepsilon = 0.96$, and $\varepsilon = 0.98$. (For interpretation of the references to colour in this figure legend, the reader is referred to the web version of this article.)

u_*. However, we do not see similar patterns of kB^{-1} at forested sites. Even though there are large dynamics in daytime u_* at forests, kB^{-1} is relatively constant during the daytime over these land covers. Visually, this suggests a weaker relationship between kB^{-1} and u_* at forested sites. Croplands exhibit variations in both daytime kB^{-1} and r_b, however, the temporal patterns do not visually match the temporal variations in u_*.

3.2. Dependence of kB^{-1} on u_*

Recall, when quantitatively determining the relationship between kB^{-1} and u_*, we subsampled the data to include only the 8 half-hours with the largest sensible heat flux for each day. Using this subsample of data, we calculated the correlation between kB^{-1} and u_* at each site. We grouped the correlations by land cover type, as shown in Fig. 2a and b. All land cover types exhibit small and negative correlations between r_b and u_* (Fig. 2a). However, patterns emerge when assessing the correlation between u_* and kB^{-1} (Fig. 2b). On average, shrublands exhibited the highest correlation between kB^{-1} and u_* (median = 0.64), followed by grasslands (median = 0.36). Crops and deciduous broadleaf forests had lower correlations between kB^{-1} and u_* (median = 0.04 and 0.04, respectively), with some sites exhibiting negative correlations. Although the average correlation between kB^{-1} and u_* across evergreen needleleaf forests was also low (median = 0.20), the strength of the relationship between varied across sites, with correlations ranging from −0.20 to 0.86.

As the second metric to assess the relationship between r_b, kB^{-1}, and u_*, we fit a power law model to the half-hourly data at each site in the form $r_b = a(u_*^{P1})$ and $kB^{-1} = b(u_*^{P2})$. In these equations, positive values of $P1$ and $P2$ indicate a positive relationship between r_b and u_* and kB^{-1} and u_*, respectively. Additionally, the magnitude of $P1$ and $P2$ indicates the strength of the relationship between r_b and u_* and kB^{-1} and u_*, while the coefficients a and b are scaling parameters. Results of this fit are consistent with the correlation analysis, as shown in Fig. 2c and d. Specifically, $P1$ tends to be negative, indicating an inverse relationship between r_b and u_*. Additionally, shrublands and grasslands are associated with the smallest magnitude of $P1$, but the largest magnitude of $P2$. Croplands and forested sites have moderate values of $P1$ and $P2$. Interestingly, the median values of $P2$ are all between 0.48 (croplands) and 0.95 (shrublands). However, as shall be seen later, parameterizations with $P2 = 0.25$ almost yielded errors of the same order of magnitude as those with $P2 = 0.50$ when a free parameter in each parameterization (e.g., the b in $kB^{-1} = bu_*^{P2}$) is calibrated.

Lastly, using the same subset of data, we investigated the relationship between kB^{-1} and u_* through the Re_*, as shown in Fig. 3. The 2-dimensional histogram in Fig. 3 reveals no discernable scaling relationship between kB^{-1} and Re_*. Additionally, there is no relationship between site-averaged kB^{-1} and site-averaged Re_* at the 74 sites. Although the average Re_* varies across land cover types, the average kB^{-1} is relatively constant at approximately 2.7, as shown by the large symbols in Fig. 3. Recall, Re_* is a function of u_* and z_o, which is assumed to be 10% of the vegetation height. The dependence on vegetation height is seen here as two groupings of data that reflect varying vegetation heights. Specifically, values associated with short vegetation (shrublands and grasslands) are centered around $\log_{10}(Re_*) \approx 3.4$and $kB^{-1} \approx 4.4$, while values associated with tall vegetation (deciduous and evergreen forests) are centered around $\log_{10}(Re_*) \approx 4.8$and $kB^{-1} \approx 1.3$. Croplands, which are represented by triangles in Fig. 3, have intermediate values between the shrublands/grasslands and forested sites.

3.3. Parameterizing kB^{-1}

Using daytime ($H > 20\ \mathrm{Wm}^{-2}$) data from 74 AmeriFlux sites, we re-calibrated previously proposed models of kB^{-1} for each land cover type by minimizing the RMSE between predicted and observed surface temperatures. After estimating the RMSEs, we averaged the RMSEs across land cover type and determined the coefficients (C_1, C_2, C_3, L_{w1} and L_{w2}) associated with the minimum RMSE for each land cover, as shown by the colored lines in Fig. 4, as well as for all 74 sites, as shown by the black line in Fig. 4. For reference, we also calibrated a constant kB^{-1} and a constant z_{oh}, which are also aggregated by land cover type

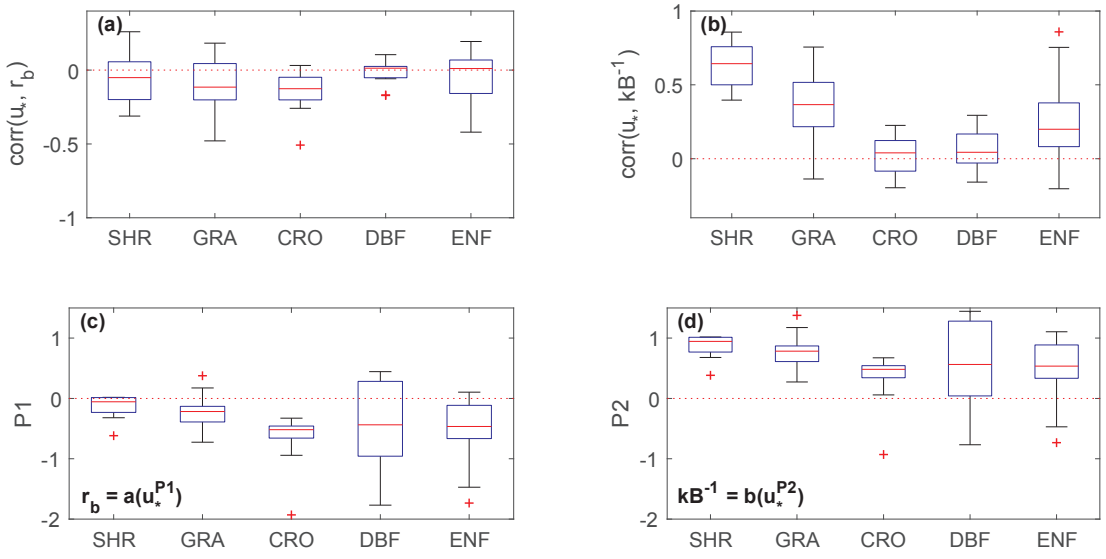

Fig. 2. The relationship between z_{oh} and u_* with $\varepsilon = 0.98$ in terms of (a) the Pearson correlation coefficient of u_* and r_b, estimated from a subset of data including the 8 half-hours of maximum sensible heat flux each day in summer. For each box, the red line represents the median and the top and bottom edges of the box represent the 75th and 25th percentiles, respectively. The whiskers encompass the range of data not considered outliers and the outliers are plotted as red '+' symbols; (b) same as (a), but between $u_*$and kB^{-1}; (c and d) fit power functions with the functional form indicated in the bottom left panel of the subplot. Similar figures with $\varepsilon = 0.94$ and $\varepsilon = 0.96$ are shown in Appendix A. (For interpretation of the references to colour in this figure legend, the reader is referred to the web version of this article.)

similarly, as shown in Fig. 4a and b.

The patterns displayed in Fig. 4 tend to follow the relationship, or lack of relationship, between kB^{-1} and u_* described above in Section 3.2; specifically, the forested and cropland sites behave different than the grasslands and shrublands. Values associated with the minimum RMSE, i.e. the circular points in Fig. 4, are listed for each land cover type in Table 2 for all three ε values (0.94, 0.96, 0.98). As shown in Table 2, the magnitudes of these values (kB^{-1}, z_{oh}, L_{w1}, L_{W2}, C_1, C_2, and C_3) are sensitive to ε, which is consistent with Eq. 5 and Eq. 6. Although the magnitudes are dependent on ε, the relative patterns across land cover are consistent. When comparing the land covers, coefficients C_1 and C_2 are lower at forested and cropland sites compared to shrublands and grasslands. Additionally, coefficient C_3 is often negative at the forested sites, indicating that, on average, there is an inverse relationship between daytime kB^{-1} and u_* at these locations. For all C_1, C_2, and C_3, errors in temperature tend to be more sensitive to perturbations in the coefficients, as demonstrated by the slope of the green and purple lines in Fig. 3d-e compared to the red, blue, and green. The leaf boundary layer model associated with L_{w2} (dashed lines on Fig. 4c), on the other hand, has a relatively flat error function across all land cover types, signifying that the model is relatively insensitive to variations in L_{w2}.

When holding kB^{-1} constant, smaller kB^{-1} values tend to minimize RMSEs in temperature at forested sites ($kB^{-1} = 0.25$ to 0.75, $\varepsilon = 0.98$) compared to croplands ($kB^{-1} = 1.75$, $\varepsilon = 0.98$), grasslands ($kB^{-1} = 2.5$, $\varepsilon = 0.98$), and shrublands ($kB^{-1} = 3.5$, $\varepsilon = 0.98$).

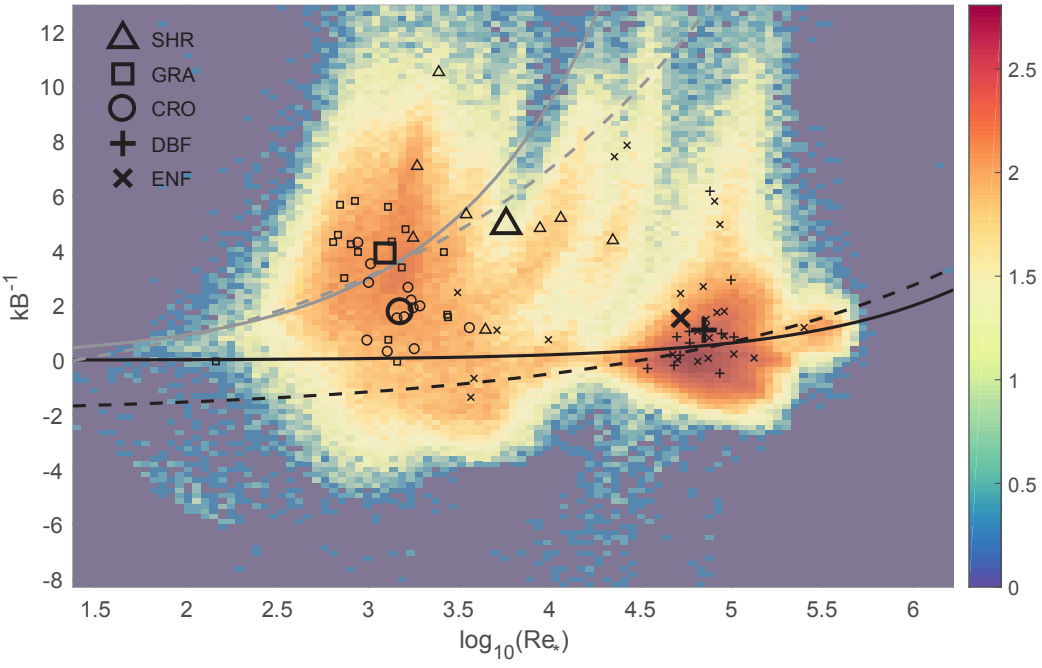

Fig. 3. Two-dimensional histogram of $\log_{10}(Re_*)$ and kB^{-1} across all 74 AmeriFlux sites during the summer daytime with $\varepsilon = 0.98$. The background color and associated color bar represent the histogram, i.e. number of half-hours of data, on a log scale. Small symbols represent site-specific averages, while the large symbols represent the average across land cover types. The shape of the symbol indicates the land cover type, with triangles representing shrublands, squares representing grasslands, circles representing croplands, plus signs representing deciduous broadleaf forests, and crosses representing evergreen needleleaf forests. The gray and black solid lines represent the maximum and minimum C_1(=0.15, 0.90) in Eq. (10) from Table 2 ($\varepsilon = 0.98$), respectively. The gray and black dashed lines represent the maximum and minimum C_2(=0.002, 0.094) in Eq. (11) from Table 2 ($\varepsilon = 0.98$), respectively. Similar figures with $\varepsilon = 0.94$ and $\varepsilon = 0.96$ are shown in Appendix A. (For interpretation of the references to colour in this figure legend, the reader is referred to the web version of this article.)

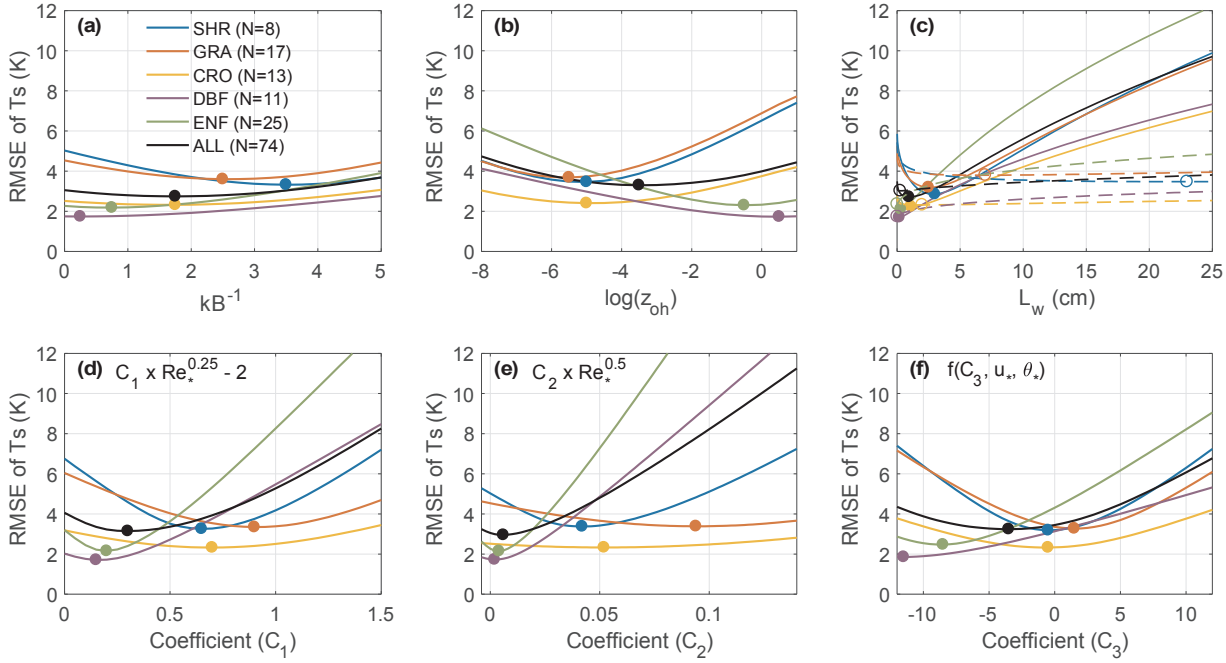

Fig. 4. RMSEs associated with temporally constant (a) kB^{-1}, (b) z_{oh}, (c) L_{w1} (solid line with filled circles) and L_{w2} (dashed line with open circles), (d) C_1, (e) C_2, and (f) C_3 aggregated across land cover types with $\varepsilon = 0.98$. Land cover types are indicated by color as described in panel (a), with shrublands in blue, grasslands in red, croplands in gold, deciduous broadleaf forests in purple, evergreen needleleaf forests in green, and the across all site average in black. The points represent the minimum RMSE and are listed in Table 2 for $\varepsilon = 0.94$, 0.96, and 0.98.

Table 2
The constant kB^{-1}, $\ln(z_{oh})$, L_{w1}, L_{w2}, C_1, C_2, and C_3 associated with the minimum RMSE for each land cover, as represented by the points in Fig. 4, for each emissivity (0.94, 0.96, and 0.98).

	kB^{-1}	$\ln(z_{oh})$	L_{w1}	L_{w2}	C_1	C_2	C_3
Emissivity = 0.94							
SHR	4	-5.5	3.50	40	0.7	0.048	0.5
GRA	3	-6	3.50	12	1	0.110	2.5
CRO	2	-5	1.48	4	0.75	0.062	0
DBF	0.5	0	0.28	0.021	0.2	0.004	-11
ENF	1	-1	0.46	0.021	0.25	0.006	-8
ALL	2.25	-4	1.26	0.541	0.35	0.008	-2.5
Emissivity = 0.96							
SHR	3.75	-5.5	3.00	30	0.7	0.046	0
GRA	2.75	-6	3.00	9	0.95	0.102	2
CRO	1.75	-5	1.28	3	0.75	0.058	-0.5
DBF	0.5	0	0.22	0.021	0.2	0.004	-11.5
ENF	1	-0.5	0.36	0.021	0.2	0.004	-8.5
ALL	2	-3.5	1.08	0.36	0.3	0.006	-3
Emissivity = 0.98							
SHR	3.5	-5	3.00	23	0.65	0.042	-0.5
GRA	2.5	-5.5	2.50	7	0.9	0.094	1.5
CRO	1.75	-5	1.10	2	0.7	0.052	-0.5
DBF	0.25	0.5	0.18	0.021	0.15	0.002	-11.5
ENF	0.75	-0.5	0.30	0.021	0.2	0.004	-8.5
ALL	1.75	-3.5	0.94	0.26	0.3	0.006	-3.5

Similarly, the calibrated z_{oh} values at forests (z_{oh} = 0.61 to 1.6 m, $\varepsilon = 0.98$) tended to be higher compared to croplands and shrublands (both z_{oh} = 0.0067 m, $\varepsilon = 0.98$), and grasslands (z_{oh} = 0.0041 m, $\varepsilon = 0.98$). When ε decreases, kB^{-1} increases and $\log(z_{oh})$ decreases as shown in Table 2.

The minimal RMSE values associated with each model and each land cover type are shown in Fig. 5. In general, the RMSE values at the croplands and forested sites remained relatively constant regardless of model, while the RMSE values at the grasslands and shrublands varied depending on the specific model, as shown by the colored bars in Fig. 5. The hatched bars (plotted on top of the colored bars in Fig. 5) represent the standard deviation (STDEV) of the errors. When compared to the total RMSE values across land cover types, the hatched bars provide information on the amount of error resulting from variability rather than bias. For example, at the shrubland sites, the Re_* power function with exponent equal to 0.5 (Eq. 11, "Constant C_2" in Fig. 5 legend) has a higher RMSE compared to the "Constant C_1" (Eq. 10) and "Constant C_3" models (Eq. 12), but not the highest STDEV, indicating the model has more bias contributing to the error than the other models. With respect to average temperature errors, the constant kB^{-1} model generally had slightly smaller errors that the constant z_{oh} model.

4. Discussion

4.1. Errors associated with inferred kB^{-1}

It is important to recognize that kB^{-1} cannot be directly measured and must be inferred from surface flux and meteorological measurements coupled with Monin-Obukhov similarity theory or some other models. Thus, errors in flux and meteorological measurements, as well as errors in model structure and parameterizations, are propagated to kB^{-1}. These errors are particularly evident during the nighttime. For example, we found that the inferred kB^{-1} values at nighttime were strongly sensitive to emissivity (Figs. S1-S3), indicating that robust inferences cannot be drawn from nighttime results when emissivity is unknown. Additionally, kB^{-1} was often less than zero during the nighttime (Fig. 3), implying that $z_{oh} > z_o$ and, thus, negative r_b. Although many previous studies have reported similar negative kB^{-1} values during the nighttime (Liu et al., 2015; Su et al., 2001; Verhoef et al., 1997; Yang et al., 2008), negative resistances imply that momentum transfer is less efficient than heat transfer, which is not physically realistic. Thus, negative kB^{-1} values are often attributed to measurements errors in ancillary data, an over-simplification of Eq. 4 for complex surfaces, such as natural vegetation (Su et al., 2001), and/or the breakdown of Monin-Obukhov similarity theory because of interactions between active and inactive turbulence in the surface layer (Yang et al., 2008). Thus, to minimize the error associated with small temperature gradients and nighttime errors, we restricted our analysis to the daytime ($H > 20\ Wm^{-2}$), and further subsampled the data when determining the dependence of kB^{-1} on u_* (the 8 half-hours of the day

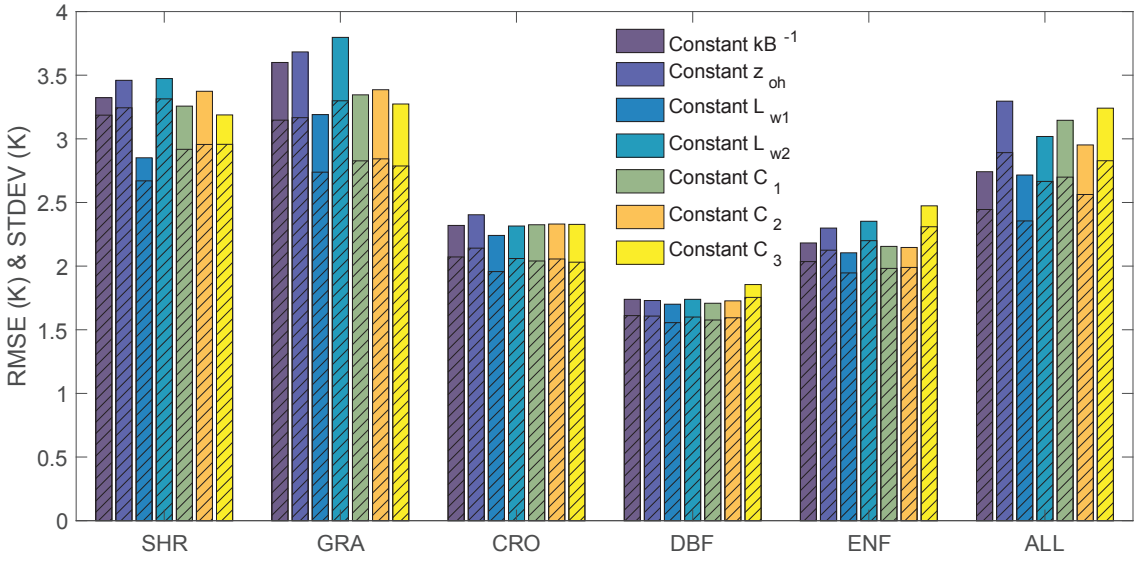

Fig. 5. RMSEs of computed T_s and standard deviations (STDEV; hatched bars) associated with different kB^{-1} in Fig. 4 (with $\varepsilon = 0.98$). Bars are grouped by land cover type and colored by constants, as shown in the legend. The number of sites (N) aggregated for each land cover type is located below each land cover type. Similar figures with $\varepsilon = 0.94$ and $\varepsilon = 0.96$ are shown in Appendix A. (For interpretation of the references to colour in this figure legend, the reader is referred to the web version of this article.)

with the largest sensible heat flux).

It is also important to note that the daytime kB^{-1} values also depend on the emissivity value (Eq. 6), which is unknown. For a given land cover type the inferred kB^{-1} increases with decreasing emissivity values (Table 2). Uncertainties in the emissivity thus introduce ambiguity in the exact kB^{-1}value to be recommended for use in large-scale models. Errors associated with the viewing angle of the radiometer are not considered here but are likely to also induce uncertainties in the inferred kB^{-1} (Matsushima and Kondo, 1997). However, the relative variations between land cover types are consistent across emissivities. For example, when a constant kB^{-1} is assigned to each land cover to minimize the errors in computed surface temperatures, this kB^{-1} value tends to be smaller at forested sites than at shrublands/grasslands, with intermediate values at croplands (Table 2)

4.2. Dependence of kB^{-1} on u_*

From the inferred kB^{-1} estimates, we investigated the correlation between u_* and kB^{-1} across varying land cover types. We anticipated land cover dependence of kB^{-1} because kB^{-1} should depend on the bulk geometry of surface and the source/sink positions in the canopy, e.g. fraction and distribution of leaves (Garratt, 1994). During the daytime, u_* and kB^{-1} both increase at shrublands and grasslands, as shown in Fig. 1; however, forests tend towards constant kB^{-1} during the daytime. At croplands kB^{-1} generally increases throughout the day, but does not decline in the afternoon similar to u_*. Quantitatively, our results suggest a stronger relationship between u_* and kB^{-1} over shrubland/grassland sites compared to croplands/forest sites, as shown in Fig. 2. Brutsaert and Stricker (1979) found similar results when comparing a grassland site to a forest site, noting that kB^{-1} was relatively insensitive to u_* and independent of z_o over a forest site with dense vegetation because flow above the forest canopy primarily interacts with the top of the canopy rather than the leaves and the soil surface below.

We also calculated the correlation between u_* and r_b and found minimal correlations across all land cover types (Fig. 2a). These results are generally consistent with Eq. (3). Specifically, as demonstrated by Eq. (3), if r_b were constant, we would expect kB^{-1} to be u_* dependent; while if r_b scaled inversely with u_*, then we would expect a constant kB^{-1}. However, although the median diurnal kB^{-1} values are consistent with the observed relation between the median diurnal r_b and median diurnal u_*, the covariance of diurnal median r_b and diurnal median u_* (Fig. 1) is inconsistent with the power-law fits and inter-day correlations (Fig. 2). For example, we see strong positive diurnal covariance between r_b and u_* at shrublands in Fig. 1, but weak covariance of r_b and u_* between days in Fig. 2. This could be due to either diurnal biases in the radiometric estimate of T_s (e.g. due to angle dependent emissivity), mixed soil vegetation effects, or diurnal biases in the diffusion model (e.g. in the u_*, T_a, and H dependent Obukhov length) introducing diurnal biases in r_b through Eqs. (1), (7), and (8). Recall, kB^{-1} is a definitional quantity fictitiously used to extend the turbulent profiles into laminar sub-layer (Brutsaert, 2005). In Eq. (5), we are fundamentally estimating r_b and, in the process, defining kB^{-1} such that an artificial dependence on u_* is introduced.

If we treat shrublands/grasslands as bluff body roughness elements and croplands/forests as permeable, well-packed roughness elements, our results agree well with the previous literature. For example, Garratt (1994) found that, for surfaces with bluff elements, kB^{-1} scales with Re_*; however, for surfaces with permeable or randomly distributed elements, kB^{-1} is almost independent of Re_*, and can be assumed to be approximately 2. Across all land cover types, (Garratt, 1994) found little variations in kB^{-1} with Re_*, with a relatively constant average kB^{-1}, as also demonstrated here in Fig. 3.

The contrasting dependence of kB^{-1} on measured u_* over shrubland/grassland and cropland/forest sites appears to be consistent with numerical and experimental investigations of turbulent structures over sparsely and dense canopies (see Raupach and Thom, 1981; Finnigan, 2000; Belcher et al., 2012 for reviews). It is now well recognized that when there is no canopy or when the canopy density is low (e.g., shrublands and grasslands), the atmospheric flow over the land surface resembles a rough wall boundary layer. However, in the case of dense canopies over the land surface (e.g., forests and croplands), the atmospheric flow and turbulent transport are significantly altered and a mixing layer is developed at the canopy top (Raupach et al., 1996; Poggi et al., 2004; Finnigan et al., 2009). As a result, the measured statistics above the canopy do not represent the turbulent characteristics inside the canopy due to the 'blocking' effect of the mixing layer (Raupach et al., 1996; Poggi et al., 2004; Finnigan et al., 2009). It is thus understandable why kB^{-1} over forests/croplands is less correlated with variations in the measured u_*.

4.3. Parameterizations of kB^{-1}

When comparing parameterizations of kB^{-1}, our results suggest similar RMSEs in the computed surface temperature regardless of the model, as shown in Fig. 5. Thus, we cannot strongly recommend one model for use in large-scale models. Recall, we have calibrated one free parameter in each model depending on land cover type, as shown in Fig. 4. Patterns emerge when assessing the magnitude of the parameters C_1, C_2, and C_3, specifically with forests and croplands displaying smaller C_1 and C_2 values compared to shrublands and grasslands. For forested sites, C_3 is even negative. These findings are consistent with the finding that kB^{-1} in forests/croplands is not dependent on the measured u_* above the canopy, as previously discussed.

However, our results do show that the leaf boundary layer model is less sensitive in the calibration of L_{w2} than other models (Fig. 4c), which minimal changes in RMSE as the free parameter diverges from the optimal. In general, for shrublands and grasslands, using a kB^{-1} model with velocity dependence tends to reduce RMSEs. However, if u_* is not measured, as at eddy covariance sites, it may be useful to use a constant kB^{-1} (with recommended values in Table 2) or the leaf boundary layer model. Note that the formulation of Yang et al. (2008) requires H to be an input for modeling z_{oh}, as shown in Eq. (13) through its dependence on L, and thus z_{oh} would need to be estimated iteratively in modeling applications.

5. Conclusion

In summary, our analysis synthesizes the relationship between kB^{-1} and u_* across land cover types using a vast amount of eddy covariance data (i.e., more that 250 thousand observations across 74 sites post-subsampling for the 8 half-hour in each day with the largest H). We find the kB^{-1} values at shrublands and grasslands to be well correlated with measured u_*, while kB^{-1} values at forests and croplands are independent of measured u_*. This is consistent with the contrasting features of turbulent structures over sparse and dense vegetation canopies. Additionally, our results suggest that kB^{-1} parameterizations lead to similar RMSE values when one free parameter is calibrated. When comparing the calibrated parameters (C_1, C_2, and C_3) in kB^{-1} parameterizations across land covers, the strength of the correlation between kB^{-1} on u_* is reflected in the magnitude/sign of the coefficients.

Funding sourcesFunding sources

This material is based upon work supported by the National Science Foundation (NSF) under grant DGE-1247312.

Acknowledgements

We thank the AmeriFlux primary investigators of the sites in this study whose work made this research possible, including: B. Amiro, M. Arain, J. Baker, D. Baldocchi, C. Bernacchi, D. Billesbach, S. Biraud, P. Blanken, G. Bohrer, J. Bradford, N. Brunsell, J. Chen, K. Clark, P. Curtis, A. Desai, S. Dore, B. Ewers, C. Gough, T. Griffis, L. Gu, D. Hollinger, T. Kolb, B. Law, M. Litvak, H. Margolis, W. J. Massman, J. McFadden, T. Meyers, A. Noormets, K. Novick, C. Oishi, S. Papuga, T. Parkin, E. Pendall, R. Phillips, J. Prueger, R. Scott, P. Stoy, A. Suyker, R. Suzuki, M. Torn, S. Wharton, and J. Wood. Funding for many of these sites was provided by the U.S. Department of Energy's Office of Science and the Ameriflux Network Management Project, Fluxnet-Canada, and/or the Canadian Carbon Program. AmeriFlux data are available at http://ameriflux.ornl.govhttp://ameriflux.ornl.gov

Appendix A. Supplementary data

Supplementary data associated with this article can be found, in the online version, at http://dx.doi.org/10.1016/j.agrformet.2017.06.003.

References

Belcher, S.E., Harman, I.N., Finnigan, J.J., 2012. The Wind in the Willows: Flows in Forest Canopies in Complex Terrain. Annual Review of Fluid Mechanics 44, 479–504. http://dx.doi.org/10.1146/annurev-fluid-120710-101036.

Blumel, K., 1999. A simple formula for estimation of the roughness length for heat transfer over partly vegetated surfaces. J. Appl. Meteor. 38 (10), 814–829. http://dx.doi.org/10.1175/1520-0450(1999)038<0814:ASFFEO>2.0.CO;2.

Brutsaert, W., Stricker, H., 1979. An advection-aridity approach to estimate actual regional evapotranspiration. Water Resour. Res. 15, 443–450. http://dx.doi.org/10.1029/wr015i002p00443.

Brutsaert, W., 1982. Evaporation into the Atmosphere: Theory, History and Applications. Springer Netherlands, Netherlands.

Brutsaert, W., 2005. Hydrology. Cambridge University Press, New York NY.

Chamberlain, A.C., 1966. Transport of gases to and from grass and grass-Like surfaces. Proc. R. Soc. London. Ser. A, Math. Phys. Sci. 290, 236–265.

Chaney, N.W., Herman, J.D., Ek, M.B., Wood, E.F., 2016. Deriving global parameter estimates for the noah land surface model using FLUXNET and machine learning. J. Geophys. Res. http://dx.doi.org/10.1002/2016jd024821.

Defraeye, T., Verboven, P., Ho, Q.T., Nicolai, B., 2013. Convective heat and mass exchange predictions at leaf surfaces: applications, methods and perspectives. Comput. Electron. Agric. 96, 180–201. http://dx.doi.org/10.1016/j.compag.2013.05.008.

Finnigan, J.J., 2000. Turbulence in Plant Canopies. Annual Review of Fluid Mechanics 519–571.

Finnigan, J.J., Shaw, R.H., Patton, E.G., 2009. Turbulence structure above a vegetation canopy. J. Fluid Mech. 637, 387. http://dx.doi.org/10.1017/S0022112009990589.

Garratt, J.R., 1994. The Atmospheric Boundary Layer, 1st ed. Cambridge University Press, Cambridge.

Kanda, M., Kanega, M., Kawai, T., Moriwaki, R., Sugawara, H., 2007. Roughness lengths for momentum and heat derived from outdoor urban scale models. J. Appl. Meteor. Climatol. 46, 1067–1079. http://dx.doi.org/10.1175/jam2500.1.

Lhomme, J.P., Troufleau, D., Monteny, B., Chehbouni, A., 1997. Sensible heat flux and radiometric surface temperature over sparse Sahelian vegetation II. A model for the kB- 1 parameter. J. Hydrol. 188–189, 839–854. http://dx.doi.org/10.1016/s0022-1694(96)03173-3.

Liu, Y., Guo, W., Song, Y., 2015. Estimation of key surface parameters in semi-arid region and their impacts on improvement of surface fluxes simulation. Sci. China Earth Sci. 59, 307–319. http://dx.doi.org/10.1007/s11430-015-5140-4.

Massman, W.J., 1999. A model study of kBH-1 for vegetated surfaces using localized near-field Lagrangian theory. J. Hydrol. 223, 27–43. http://dx.doi.org/10.1016/s0022-1694(99)00104-3.

Matsushima, D., Kondo, J., 1997. A proper method for estimating sensible heat flux above a horizontal-homogeneous vegetation canopy using radiometric surface observations. J. Appl. Meteor. 36, 1696–1711.

Monteith, J., Unsworth, M., 2013. Principles of Environmental Physics, 4 ed. Academic Press Oxford, UK.

Owen, P.R., Thomson, W.R., 1963. Heat transfer across rough surfaces. J. Fluid Mech. 15, 321–334.

Parlange, J.Y., Waggoner, P.E., 1972. Boundary layer resistance and temperature distribution on still and flapping leaves II. Field experiments. Plant Physiol. 50, 60–63.

Parlange, J.Y., Waggoner, P.E., Heichel, G.H., 1971. Boundary layer resistance and temperature distribution on still and flapping leaves I: Theory and laboratory experiments. Plant Physiol. 48, 437–442.

Pennypacker, S., Baldocchi, D.D., 2016. Seeing the fields and forests: application of surface-Layer theory and flux-Tower data to calculating vegetation canopy height. Boundary-Layer Meteorol. 158, 165–182. http://dx.doi.org/10.1007/s10546-015-0090-0.

Poggi, D., Porporato, A., Ridolfi, L., Albertson, J.D., Katul, G.G., 2004. The Effect of Vegetation Density on Canopy Sub-Layer Turbulence. Boundary-Layer Meteorol 111, 565–587. http://dx.doi.org/10.1023/B:BOUN.0000016576.05621.73.

Raupach, M.R., Finnigan, J.J., Brunet, Y., 1996. Coherent eddies and turbulence in vegetation canopies: The mixing-layer analogy. Boundary-Layer Meteorol 78, 351–382.

Raupach, M.R., Thom, A.S., 1981. Turbulence in and Above Plant Canopies. Annual Review of Fluid Mechanics 13, 97–129.

Rigden, A.J., Salvucci, G.D., 2015. Evapotranspiration based on equilibrated relative humidity (ETRHEQ): Evaluation over the continental U.S. Water Resour. Res. 51, 2951–2973. http://dx.doi.org/10.1002/2014WR016072.

Su, Z., Schmugge, T., Kustas, W.P., 2001. An evaluation of two models for estimation of the roughness height for heat transfer between the land surface and the atmosphere. J. Appl. Meteor. 40 (10), 1933–1951. http://dx.doi.org/10.1175/1520-0450(2001)040<1933:AEOTMF>2.0.CO;2.

Thom, A.S., 1972. Momentum, mass and heat exchange of vegetation. Q. J. R. Meteorol. Soc. 98, 124–134. http://dx.doi.org/10.1002/qj.49709841510.

Verhoef, A., De Bruin, H.A.R., Van Den Hurk, B.J.J.M., 1997. Some practical notes on the parameter kB(-1) for sparse vegetation. J. Appl. Meteor. 36 (10), 560–572. http://dx.doi.org/10.1175/1520-0450(1997)036<0560:SPNOTP>2.0.CO;2.

Yang, Friedl, M.A., 2003. Determination of roughness lengths for heat and momentum over boreal forests. Boundary-Layer Meteorol. 107, 581–603. http://dx.doi.org/10.1023/A:1022880530523.

Yang, Koike, Ishikawa, T., Kim, H., Li, J., Liu, X., Liu, H., Ma, S., Wang, Y., 2008. Turbulent flux transfer over bare-soil surfaces: characteristics and parameterization. J. Appl. Meteor. Climatol. 47, 276–290. http://dx.doi.org/10.1175/2007jamc1547.1.

Zilitinkevich, S., 1995. Non-local turbulent transport: pollution dispersion aspects of coherent structure of connective flows. Trans. Ecol. Environ. 6, 1743–3541. http://dx.doi.org/10.2495/AIR950071.